A Direct Transition State Theory Based Study of Methyl Radical Recombination Kinetics

Stephen J. Klippenstein*

Chemistry Department, Case Western Reserve University, Cleveland, Ohio 44106-7078

Lawrence B. Harding*

Theoretical Chemistry Group, Argonne National Laboratory, 9700 South Cass Avenue, Argonne, Illinois 60439

Received: May 14, 1999; In Final Form: July 26, 1999

Multireference configuration interaction based quantum chemical estimates are directly implemented in a variational transition state theory based analysis of the kinetics of methyl radical recombination. Separations ranging from 5.5 to 1.9 Å are considered for two separate forms for the reaction coordinate. The a priori prediction for the high-pressure limit rate constant gradually decreases with increasing temperature, with a net decrease of a factor of 1.7 from 300 to 1700 K. Near room temperature, this theoretical estimate is in quantitative agreement with the experimental data. At higher temperatures, comparison between theory and experiment requires a model for the pressure dependence. Master equation calculations employing the exponential down energy transfer model suggest that the theoretical and experimental high-pressure limits gradually diverge with increasing temperature, with the former being about 3 times greater than the latter at 1700 K. The comparison with experiment also suggests that the energy transfer coefficient, $\langle \Delta E_{down} \rangle$, increases with increasing temperature.

I. Introduction

The accurate a priori prediction of rate constants for reactions of polyatomic species remains a difficult and important goal. One of the primary difficulties involves the development of sufficiently accurate representations of the multidimensional potential energy surface. Direct dynamics approaches (see, e.g., refs 1−3) bypass one aspect of this difficulty by obtaining an ab initio quantum chemical estimate of the potential for each configuration sampled in the dynamics. One is then limited only by the accuracy of the underlying quantum chemical evaluations and dynamical simulations. Unfortunately, such direct dynamical procedures generally require vast CPU times due to the enormous number of potential energy evaluations in typical dynamical simulation procedures. The representation of the potential in terms of an expansion about some selected geometries provides one route for reducing the number of ab initio energetic evaluations.[4,5]

Alternatively, replacing the dynamical simulation with a transition state theory (TST) based simulation can yield an even greater reduction in the number of required calls to the potential. For example, within reaction path Hamiltonian based approaches, one typically requires only the potential, its gradient, and its second derivative, at a limited number of points along the reaction path.[6,7] For barrierless reactions the situation is more complicated since many of the modes are in the process of changing from free rotors to nearly harmonic bending motions. As a result, simple quadratic representations of the potential and the corresponding rigid-rotor harmonic oscillator estimates for the energetics seem inadequate.

Phase space integral based representations of the transition state partition function have provided a means for accurately treating the anharmonicities and kinetic couplings of these "transitional" modes, but require a global potential for them.[8,9] However, with Monte Carlo integration techniques one may obtain reasonably well converged results with only a limited number of configurational samplings and corresponding potential energy evaluations. For example, convergence to about 10% can be obtained with simple random sampling of about 1000 sets of the transitional mode coordinates.[10] Consideration of about 10 different reaction coordinates will often provide a reasonably satisfactory optimization of the transition state dividing surface. Thus, a total of about 10^4 ab initio evaluations may be used to obtain direct variational TST estimates for the rate constant which include the full anharmonicity and mode−mode couplings for the transitional modes. Also, importance sampling schemes may provide a means for further reducing the number of required potential energy calls.

In this work, we present a direct TST-based study of the prototypical methyl−methyl radical recombination reaction. This reaction, which is of considerable importance in combustion processes, has been the subject of a large number of both experimental[11−20] and theoretical[16,21−42] studies. Currently available experimental measurements span the range from 200 to 1700 K with pressures ranging from 0.3 to 10^5 Torr.[43] This wide ranging experimental data set provides a valuable database for examining the quantitative accuracy of the theoretical predictions.

The present study focuses on the temperature dependence for the high-pressure limiting rate constants [$k_\infty(T)$] since an accurate understanding of this behavior is of some utility in extrapolating related experimental data from room temperature to the higher temperatures of interest in combustion chemistry. Unfortunately, the experimental studies are unable to reach the high-pressure limit for temperatures above about 400 K.[37] Thus, a direct comparison with experiment requires a model for the pressure dependence. This pressure dependence is treated here via a one-dimensional master equation[29] employing a range of energy transfer coefficients within the exponential down model.

The accuracy of the theoretical predictions for $k_\infty(T)$ depends on both the accuracy of the ab initio estimates for the potential energy surface and the validity of the statistical assumptions inherent in TST. In this work we strive to minimize the errors

10.1021/jp991574x CCC: $18.00
Published on Web 09/11/1999

in the former in order to address the latter accuracy in as meaningful a fashion as feasible. Thus, multireference configuration interaction (MR-CI) based techniques have been employed in the determination of the energetics and various corrections for basis set and geometry relaxation effects are incorporated. A detailed description of the quantum chemical methodology employed here is provided in section II. The qualitative characteristics of the potential are also summarized therein.

A meaningful analysis of the validity of TST requires an accurate procedure for evaluating the transition state partition functions. In this work, we employ the variable reaction coordinate TST formalism.[44,45] The MR-CI calculated energetics are directly incorporated in the evaluation of the phase space integrals inherent to this formalism. The details of the current implementation of the VRC-TST formalism, and of the master equation treatment of the overall kinetics, are reviewed in section III.

There have been numerous prior theoretical studies of this reaction, including ab initio quantum chemical studies of the energetics,[26,30,34,42] as well as TST-based and other model studies of the kinetics.[16,21−25,27−33,35−42] The present study proceeds susbtantially beyond these studies in a variety of ways. In particular, the ab initio energetics are generated for orders of magnitude more geometries than in any of the prior studies, and the energetics along the reaction path are generated at a higher level. Furthermore, the direct incorporation of the energetics bypasses the uncertainties in the fitting of the potential energy surfaces for the transitional modes. Finally, the modeling of the pressure dependence via a one-dimensional master equation allows for a more direct comparison of the theoretical and experimental results. This comparison is provided in section IV and some concluding remarks are then made in section V.

II. Potential Surface Calculations

A. Methodology. The basis set used in most calculations was the correlation-consistent, polarized valence double-ζ (cc-pvdz) basis set of Dunning.[46−48] All of the electronic structure results reported here come from multireference configuration interaction (MR-CI) calculations employing orbitals from complete active space, self-consistent field (CASSCF) calculations. The CASSCF reference wave function consists of two active electrons and two active orbitals (the two radical orbitals of the reactants). This is the minimum necessary to correctly describe the reactant asymptote. The CASSCF orbitals were used in multireference configuration interaction (CAS+1+2) calculations to which a multireference Davdison[49] correction was added to account for the effects of higher order excitations. To estimate the error associated with the use of the relatively small cc-pvdz basis set, additional calculations were carried out along the staggered D_{3d} path using an aug-pvtz basis set. This basis is the same as the Dunning aug-cc-pvtz basis set except that the diffuse carbon f functions and the diffuse hydrogen d functions were eliminated to make the calculations more tractable. All calculations were carried out using the COLUMBUS package of codes.[50]

One problem in doing a direct dynamics calculation using Monte Carlo methods is that the geometries are chosen randomly and consequently a starting guess for one calculation is not always appropriate for the next calculation. In doing these calculations we found 5−10% of the CASSCF calculations converged incorrectly due to poor starting guesses. However, it proved to be relatively straightforward to detect these points by monitoring the overlap of the CI wave function with the CASSCF wave function. Points having suspiciously low overlap were redone using different starting guesses.

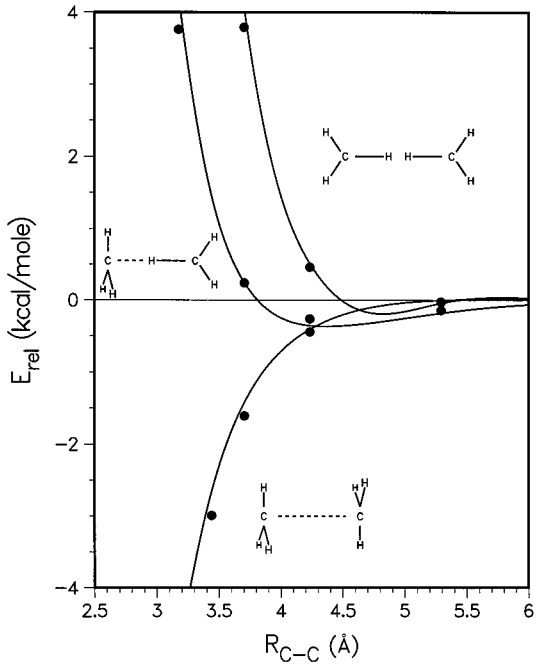

Figure 1. Plots of the energy as a function of the CC distance for three fixed orientations (as shown). The lines are the results of calculations using the cc-pvdz basis set. The solid circles denote results from aug-pvtz calculations. For all calculations the geometries of the two methyl fragments are kept frozen (planar).

B. Results. In the majority of the calculations the geometries of the two methyl radical fragments were kept frozen. Figure 1 shows comparisons of cc-pvdz and aug-pvtz calculations as a function of the C−C distance for three fixed orientations of the two methyl fragments. From this plot it can be seen that at large C−C distances (>4.5 Å) the preferred orientation is one in which one methyl fragment is perpendicular to the CC axis and the other is parallel. This is the orientation favored by the quadrupole−quadrupole interaction. At shorter distances the preferred orientation is one in which both methyl's are perpendicular to the CC axis, in a face-to-face orientation. From this plot it can also be seen that at large distances the difference between the cc-pvdz and aug-pvtz interaction energies is quite small.

To further assess the difference between the cc-pvdz and aug-pvtz results, potential curves for the face-to-face orientation were evaluated using both basis sets over a wider range of CC distances. The results are compared in Figure 2. From this plot it can be seen that the interaction energies calculated with these two basis sets are quite similar. Even at the shortest distances examined, 2.5 Å, the aug-pvtz interaction energy is only 1.1 kcal/mol (8%) more attractive. In the dynamical calculations that follow the difference between these two curves will be used as an orientation independent basis set correction to the cc-pvdz potential surfaces. Also compared in Figure 2 are potential curves with and without the Davidson correction for higher order correlations. Including the Davidson correction leads to a somewhat more attractive potential. The dynamical results reported here will employ the Davidson-corrected energies.

To assess the importance of allowing the low-frequency inversion mode of the methyl radicals to relax as the radicals approach, calculations were carried out in which the umbrella angle was optimized as a function of the CC distance. Figure 3 shows a plot of the optimum umbrella angle as a function of CC distance and Figure 4 compares the potential from this calculation to the potential obtained when the geometry of the

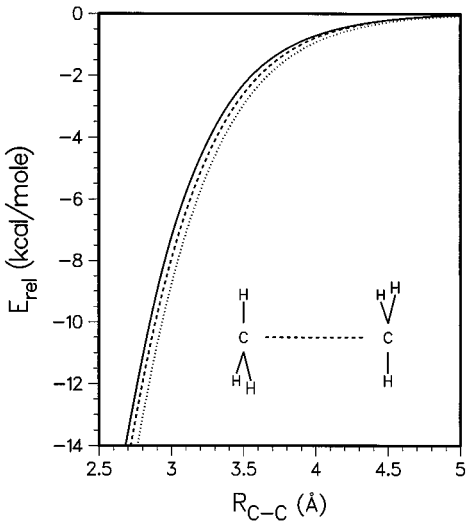

Figure 2. Plot of the energy as a function of the CC distance for the D_{3d}, face-to-face, staggered orientation (as shown). The solid line is the CAS+1+2/cc-pvdz result; the dashed line CAS+1+2/aug-pvtz; and the dotted line, CAS+1+2+QC/aug-pvtz. For all calculations the geometries of the two methyl fragments are kept frozen (planar).

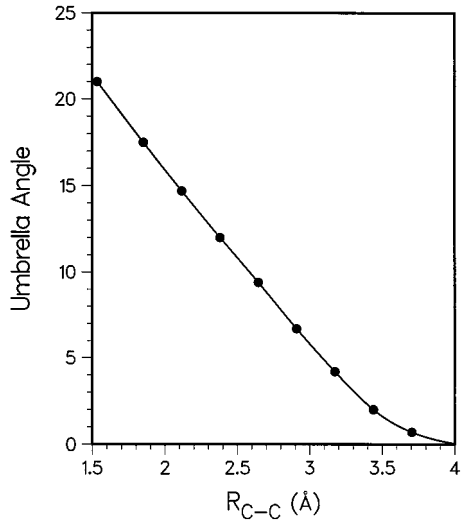

Figure 3. Optimum methyl umbrella angle as a function of the CC distance from CAS+1+2/cc-pvdz calculations. An angle of 0° corresponds to planar radicals. The molecule is constrained to be of D_{3d} symmetry.

methyl fragments is not allowed to relax. From these plots it can be seen that significant deviations from planarity start to occur at CC distances <3.5 Å. At a distance of ∼3 Å, allowing the methyls to relax leads to an interaction energy that is ∼1 kcal/mol (10%) more attractive. The difference between the two curves in Figure 4 will be used as an orientation independent correction for geometry relaxation in the dynamical calculations reported below.

To get a better understanding of the overall topology of this surface, several two-dimensional cuts were evaluated in which the CC distance was held fixed and the relative orientations of the two methyls were allowed to vary. In Figure 5 we show three plots in which the methyls are each allowed to spin about one of their CH bonds. In each case the CH bond which forms the axis of rotation is kept fixed with a CCH angle of 90° and the dihedral angle between the two axis CH bonds is fixed at 180°. For large CC distances this figure shows a potential having diagonal troughs with shallow minima at orientations where one methyl is parallel to the CC axis ($\phi = 0°$) and the other is

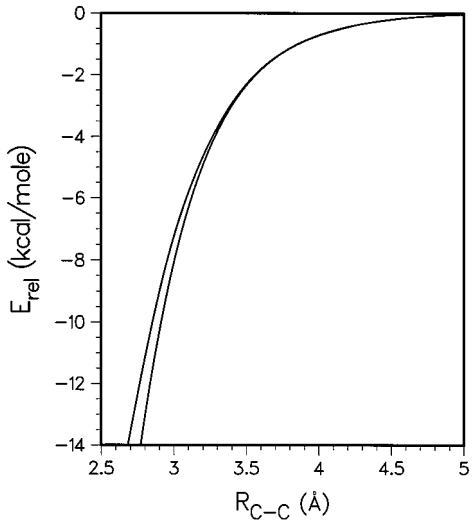

Figure 4. Comparison of D_{3d} potential curves from calculations in which the methyl radicals were kept planar (upper curve) to calculations in which methyls were allowed to distort from planarity (lower curve).

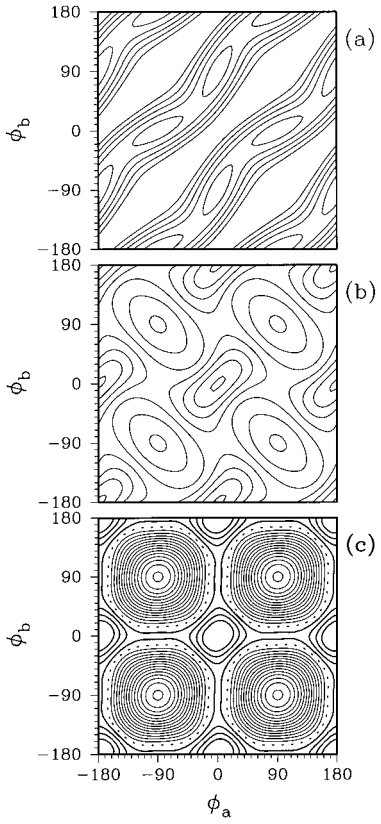

Figure 5. Contour plots of the orientation dependence of the energy for fixed CC distances. The internal geometries of the methyl radicals are kept fixed and the relative orientation of two CH bonds (C_a H_a and C_b H_b) are kept fixed with HCC angles of 90° and an H_a C_a C_b H_b dihedral angle of 180°. The plotting coordinates, ϕ_a and ϕ_b, are dihedral angles between the CH_3 planes and the CC axis (see text). Heavy solid contours denote repulsive regions (energies higher than that of the reactant asymptote), light solid contours denote attractive regions, and the dotted contours denote the energy of the reactant asymptote. The contour increments and CC distances are as follows: (a) $R_{CC} = 9$ au, inc = 0.02 kcal/mol; (b) $R_{CC} = 8$ au, inc = 0.05 kcal/mol; (c) $R_{CC} = 7$ au, inc = 0.1 kcal/mol.

perpendicular ($\phi = 90°$). As the CC distance is shortened the potential gradually deforms to one having four equivalent minima, in which both methyls are perpendicular to the CC bond. One surprising aspect of these plots is that at the shortest

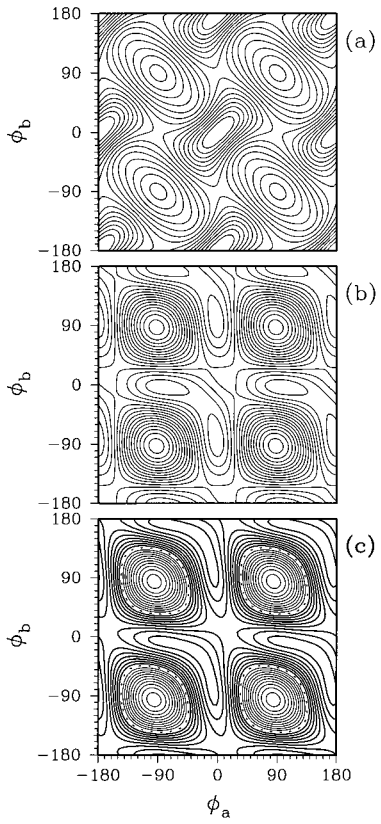

Figure 6. Same as Figure 5, only H_a CC = H_b CC=60° and $H_aC_aC_bH_b$ = 60°. The contour increments and CC distances are as follows: (a) R_{CC} = 8 au, inc = 0.02 kcal/mol; (b) R_{CC} = 7 au, inc = 0.05 kcal/mol; (c) R_{CC} = 6 au, inc = 0.2 kcal/mol.

CC distance it appears as though the preferred path to go from one of the four minima to another involves the stepwise rotation of one methyl at a time (in this plot single rotations correspond to moving either vertically or horizontally). The simultaneous rotation of both methyls in either a conrotatory (the positively sloped diagonal in the plot) or disrotatory (the negatively sloped diagonal) manner requires several kcal/mol more energy. The reason for this appears to be that in this orientation, at these relatively large CC separations, nonbonded repulsions involving the CH bonds are more important in determining the shape of the hindered-rotor potentials than covalent overlap between the two radical orbitals. This picture changes if we orient the methyls in such a way as to minimize the nonbonded repulsions. In Figure 6 we show similar plots in which the axis CH bonds are now fixed with CCH angles of 60° and the dihedral angle between the two axis CH bonds is 60°. In these plots it can be seen that for a given CC distance the hindered rotor barriers are smaller than those in Figure 5 and the disrotatory path is preferred.

To allow for an estimate of the possible contribution from the triplet state, a triplet potential curve for the face-to-face orientation was evaluated at the CAS+1+2/cc-pvdz level. This triplet curve is compared with the corresponding singlet curve in Figure 7. The splitting between these two curves is used as an orientation-independent singlet−triplet splitting in generating a crude triplet potential energy surface for the transition state theory calculations.

III. Kinetic Methodology

A. Master Equation Formalism. The effective bimolecular rate constant for methyl radical recombination corresponds to

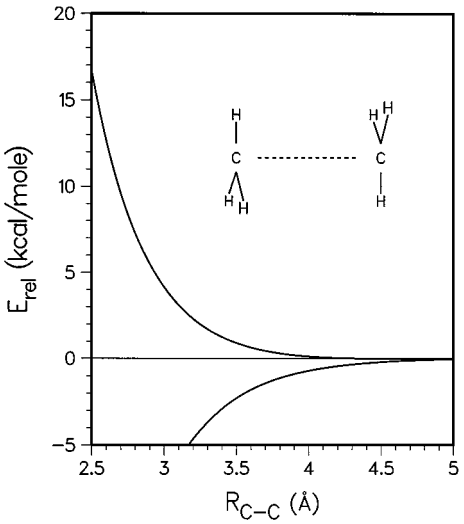

Figure 7. Comparison of CAS+1+2/cc-pvdz, D_{3d} potential curves for the singlet state (lower curve) and triplet state (upper curve). The internal coordinates of the methyl radicals are kept fixed.

a thermal average of the initial rate of formation of energized ethane complexes, $k_f(E,J)$, at energy E and total angular momentum J, times the probability of collisional stabilization at each E and J. Since a single collision does not always yield a stabilized complex, the accurate determination of the latter stabilization probability requires an analysis of the time dependence of the populations in each E and J state, as in the master equation approach.[51] For computational simplicity, a one-dimensional form of the master equation is employed here in which the J dependence of the populations is averaged over according to the scheme of Smith and Gilbert.[29]

Within this scheme, the E and J resolved dissociation rate constants, $k(E,J)$, are reduced to E resolved rate constants, $k(E)$, via the relation

$$k(E) = \frac{\int \mathrm{d}J P_{\mathrm{comp}}(J) k(E,J)/[\omega + k(E,J)]}{\int \mathrm{d}J P_{\mathrm{comp}}(J)/[\omega + k(E,J)]} \qquad (1)$$

where ω is the collision frequency, and $P_{\mathrm{comp}}(J)$ denotes the thermal equilibrium probability for the complex to have a total angular momentum of J. As discussed by Smith and Gilbert,[29] this reduction scheme, which corresponds to a strong collision assumption for the rotational degrees of freedom and assumes a decoupling of the transition probabilities in E and J, provides the correct limiting behavior in both the low- and high-pressure limits.

The present implementation of eq 1 employs the total energy and total angular momentum as variables rather than the vibrational and rotational energy employed in ref 29. These variables provide a more appropriate separation for the rate constants and are the natural variables for the present TST calculations. It is perhaps worth noting that, at least for the temperature and pressure ranges of interest here, employing the alternative reduction scheme based on simply averaging the rate constants with the $P_{\mathrm{comp}}(J)$ weighting function yields essentially identical results. However, there are other reactions where the two reduction schemes produce dramatically different results.

The time dependence of the population, P_i, of the complex in energy state i may be written as

$$\frac{dP_i}{dt} = \omega \sum_j (\mathbf{R}_{ij}P_j - \mathbf{R}_{ji}P_i) - k_i P_i + v_i \qquad (2)$$

where R_{ij} is the probability of making a transition from state i to state j during a collision with the bath gas. The first term on the right-hand side of eq 2 represents the rate of transfer from state j into state i via collisions. The second term represents the corresponding rate of transfer out of state i into state j. The third term represents the rate of loss of the complex in state i due to dissociation, while v_i is the source term describing the rate of formation of ethane in energy state i from the free methyl radicals.

The effective bimolecular rate constants are ultimately obtained via direct numerical inversion of the steady state representation of eq 2.[51] The reduced matrix procedure of ref 52 is employed and the energy transfer rate coefficients are evaluated on the basis of the exponential down model. A variety of energy transfer parameters ($\langle\Delta E_{down}\rangle$) ranging from 100 to 1600 cm^{-1} are considered since there is no suitable a priori means for obtaining quantitative estimates for the average energy transfer. For reference purposes we note here that for temperatures of 200, 296, 407, 474, 577, 810, 1305, 1525, and 1700 K, $\langle\Delta E_{down}\rangle = 100$ cm^{-1} corresponds (at the ethane dissociation threshold) to an average total energy transferred, $\langle\Delta E_{tot}\rangle$, of −40, −31, −24, −21, −17, −12, −6.2, −5.1, and −4.2 cm^{-1}, respectively. $\langle\Delta E_{down}\rangle = 200$ cm^{-1} corresponds to $\langle\Delta E_{tot}\rangle$ of −110, −94, −77, −69, −59, −43, −23, −19, and −16 cm^{-1}, respectively. $\langle\Delta E_{down}\rangle = 400$ cm^{-1} corresponds to $\langle\Delta E_{tot}\rangle$ of −290, −260, −220, −200, −180, −140, −83, −71, and −60 cm^{-1}, respectively. $\langle\Delta E_{down}\rangle = 800$ cm^{-1} corresponds to $\langle\Delta E_{tot}\rangle$ of −670, −620, −570, −540, −500, −420, −280, −240, and −210 cm^{-1}, respectively. $\langle\Delta E_{down}\rangle = 1600$ cm^{-1} corresponds to $\langle\Delta E_{tot}\rangle$ of −1460, −1400, −1330, −1290, −1230, −1100, −830, −740, and −670 cm^{-1}, respectively.

A Lennard-Jones model for the Ar···C_2H_6 collision frequency, ω, is employed (cf. eqs 5.5.14 and 5.5.17 of ref 51), with σ and ϵ values of 3.9 Å and 160 K, respectively. An energy grain size of 100 cm^{-1} provides numerically converged results for all temperatures studied here with the energies spanning the range from −20 000 cm^{-1} below to 22 000 cm^{-1} above the threshold. Total angular momentum quantum numbers ranging up to 138 are considered with a step size of 4.

The underlying dissociation rate constants, $k(E,J)$, are obtained from RRKM theory

$$k(E,J) = \frac{N^{\dagger}_{EJ}}{h\rho_{EJ}} \qquad (3)$$

where $N^{\dagger}_{EJ}$ is the transition state number of states. Rigid rotor harmonic oscillator assumptions were employed for all but the torsional mode in the evaluation of ρ_{EJ}, the density of states for the complex, and for the corresponding canonical partition function. For the torsional mode, calculations for harmonic oscillator, free rotor, and hindered rotor representations were found to differ by less than 5% for the temperatures and pressures of interest here. The pressure-dependent rate constants plotted below are for a free rotor treatment of this mode.

Symmetry numbers of 18, 72, and 72 were employed for the reactants, the transition state, and the products of the recombination reaction, respectively. The reaction was generally assumed to occur on only the ground singlet state. Thus, electronic degeneracies of 4, 1, and 1 were employed for the reactants, the transition state, and the products. Some discussion is given below of the possible contribution of the triplet state to the association kinetics.

The final results plotted here are for a dissociation energy of 87.5 kcal/mol. Various sources suggest values ranging from about 87.5 to 88.5 kcal/mol.[28] Sample calculations for the higher value were qualitatively similar yielding rates that differed by 15% or less in the range of temperature and pressures of interest here. Furthermore, the shapes of the curves were essentially identical thus yielding only a small downward shift in the magnitude of the fitted energy transfer coefficient.

B. High-Pressure Limit Rate Constant, $k_\infty(T)$. In the high-pressure limit, where the stabilization probability is unity, the effective bimolecular rate constant simplifies to

$$k_\infty(T) = \frac{1}{hQ_{\text{reactants(T)}}} \int dE\, dJ\, N_{EJ} \exp(-E/k_B T) \qquad (4)$$

where $Q_{reactants}$ is the partition function for the reactants. In TST one considers the number of available states for the motion on a dividing surface which separates reactants from products. Within a statistical framework this number of states is an upper bound to the true cumulative reaction probability. The minimum in this number of states with respect to a given family of dividing surfaces, $N^{\dagger}_{EJ}$, provides the TST approximation to the true cumulative reaction probability, N_{EJ}.

The variationally optimized dividing surface properly depends on both the total energy E and the total angular momentum J, since they are both strictly conserved between collisions. A useful simplification arises when one assumes that this transition state dividing surface depends only on temperature. In this case, the TST approximation to $k_\infty(T)$ reduces to

$$k^{\text{can}}_\infty(T) = \frac{k_B T}{h} \frac{Q^{\dagger}(T)}{Q_{\text{reactants}}(T)} \qquad (5)$$

where $Q^{\dagger}(T)$ is now the minimum in the canonical partition function for the motion on any proper dividing surface.

In the present study, the transition state number of states and rate constants are generally evaluated at the E/J resolved level. For comparison, evaluations at the canonical level yield rate constants which are typcially about 15−30% greater. The reasonably small deviation between these two quantities allows us to focus on solely the canonical variations of various factors in our qualitative discussions.

C. Variable Reaction Coordinate TST. In any recombination reaction a number of the modes transform from free rotational to nearly harmonic bending motions. In the transition state region, which typically lies at separations of about 2−5 Å, these modes are intermediate in their transformation. As a result, neither harmonic bending nor free rotational descriptions are generally correct. Instead, one must generally consider these modes as strongly coupled hindered rotors; with the extent of the hindering depending on the location of the transition state and the details of the fragment−fragment interaction potential.

Within the variable reaction coordinate TST approach[44,45] the contribution to $N^{\dagger}_{EJ}$ from these "transitional" modes is evaluated on the basis of classical phase space integrals, thereby obtaining an accurate description of the mode−mode couplings and also of angular momentum conservation. Sample calculations indicate that the quantum corrections for these modes are generally negligible due to the combination of their low effective frequency and the additional energy available from the fragment−fragment attractive interactions.[27,53] An assumed decoupling of the remaining "conserved" modes, which correspond

to the internal vibrations of the free fragments, allows for a quantum treatment of their contribution.

The transitional mode phase space integrals are evaluated here at the energy, E, and total angular momentum J resolved level according to the algorithm described in ref 45. This algorithm employs crude Monte Carlo integration and requires an interaction potential for each relative orientation of the two reacting fragments that is generated in the random sampling for a given transition state dividing surface. A prior study suggested that only a limited number of such configurational samplings (e.g., 100−1000) provide satisfactory convergence (i.e., 10%) within Monte Carlo based evaluations of these integrals.[10] This observation provided the motivation for the present direct implementation of the CAS+1+2 quantum chemical estimates for the required interactions energies.

Any implementation of transition state theory requires the specification of a dividing surface which separates reactants from products. Within variational TST one then minimizes the partition function for motion on a given dividing surface within a family of such surfaces. In this work the dividing surface is specified in terms of a fixed distance between arbitrarily chosen pivot points on each of the fragments, and two separate choices for the pivot point locations are considered. Choosing the pivot points at the centers of mass of the methyl groups provides the appropriate separation of motions at large separations and is thus a useful first choice. At shorter separations the optimum dividing surface may correspond more closely to the separation between the centers of the two radical orbitals involved in the incipient bond. Choosing the pivot points to lie 0.4 Å away from the C atoms, along the C_3 symmetry axis of the methyl fragment, should yield a reasonable first approximation to the latter dividing surface.

Ideally, one would consider a more complete set of pivot point locations (e.g., 0, 0.2, 0.4, 0.6 Å, away from the C atom). However, within the present approach, the net number of ab initio evaluations is proportional to the number of different pivot point locations considered. Thus, in the interest of computational efficiency, only the 0 (center of mass) and 0.4 Å pivot point separations were considered. For both of these choices interfragment separations ranging from 4.0 to 8.0 bohr, in 0.5 bohr spacings, were considered. For the center-of-mass reaction coordinate, larger separations of 8.5, 9.0, 9.5, 10.5, 11.5, 12.5, 14.0, and 16.0 bohr were also considered. In each case the number of configurations generated was designed to produce a net Monte Carlo integration uncertainty of about 10% or less. At the shorter separations approximately 1000 configurations were considered while only 50 configurations are required for the largest separations due to the more nearly symmetrical potential at large separations. Altogether, a total of 14 600 configurations were sampled over.

As might be expected, there is some correlation between the full interaction energy V_{int} for a given geometry and the repulsivity of the interactions between the H atoms on the two separate fragments, for that geometry. This correlation was used to obtain a modest reduction in the number of geometries for which explicit quantum chemical simulations were required. In particular, the factor

$$V_{rep} = \sum_{i,j} \exp(-0.5\ \text{Å}/r_{ij}) \qquad (6)$$

where r_{ij} is the distance between the H atoms on the separate fragments, was used as a crude representation of the repulsivity. The correlation observed in plots of V_{int} versus V_{rep} for a limited set of sampled geometries allowed for the subsequent prerejection of points with too large a V_{rep}. These prerejected points were included in the sampling but the potential was simply assumed to be infinite and no ab initio quantum chemical simulation was performed.

For large separations, little reduction could be obtained since the repulsive contribution is not dominant. However, for the shortest separation with the 0.4 Å pivot point separation, this prerejection reduced the number of required quantum chemical evaluations by a factor of 3. The sample plots also provided an extra benefit in clearly illustrating a few undetected instances where the quantum chemical simulations had converged to an incorrect electronic state. Such convergence errors were quite uncommon, occurring less than 1% of the time, and were corrected for by the generation of the appropriate energies.

A perfect separation of the conserved modes from the transitional modes and reaction coordinate would imply that the methyl radical geometry is unchanging during the course of the reaction. In reality, this geometry has a substantial variation from planar to tetrahedral during the recombination. Furthermore, the optimal geometry is a function not only of how far apart the methyl radicals are but also of their relative orientation.

In the transition state the structure tends to be more like the separated methyl radicals than like ethane. Thus, the former geometry was generally employed in the random samplings for the Monte Carlo integration of the phase space integrals. The effects of the variation in the rovibrational properties of the methyl radical were then examined and correction factors were incorporated as appropriate.

The variation in the effective moments of inertia leads to changes in the kinetic energies for the transitional modes. The variation of the product of the three moments of inertia provides a reasonable first approximation to the effect of this aspect. This product was found to vary by only about 1% from the free fragments to the transition state region and so this aspect of the variation was neglected.

A more important effect of the variation is on the interaction energies. To account for this effect, the optimum geometry and corresponding relaxation energy were determined as a function of the CC separation. This energetic relaxation was added in as an orientation independent correction to the interaction energies. The reference orientation for this correction was taken as the optimal orientation for the equivalent CC atom−atom separation. At the shorter separations, this correction is quite sizable and leads to significant varations in the estimated rate constants.

The vibrational frequencies of the conserved modes also vary along the reaction path, with that for the umbrella mode being especially large. The quantum chemical study of Robertson et al. provided GVB/3-21G estimates for the dependence of these frequencies on the CC separation.[34] This predicted variation in the conserved mode frequencies is incorporated at the harmonic oscillator level for all but the umbrella mode. For the latter mode, a one-dimensional WKB treatment is instead incorporated, again employing the data from ref 34.

The above-described correction factors are based on the optimum geometry for a given separation. In reality, the optimal geometry depends also on the relative orientation. The quantitative examination of the energetic relaxation and conserved mode vibrational frequencies for each geometry sampled in the phase space integrations is computationally intractable. However, some indication of the effect may be obtained from a limited sampling. Thus, relaxation energies and umbrella mode vibrational force fields were obtained for 39 configurations at a CC separation of 5 bohr, which corresponds to the transition state location for a temperature of 3000 K. Incorporating these relaxation energies

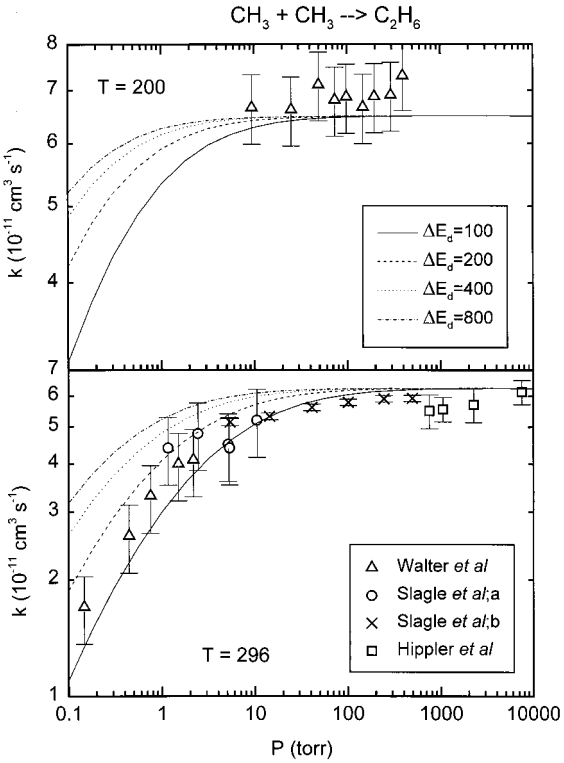

Figure 8. Plot of the pressure dependence of the rate constant for temperatures of 200 and 296 K. The squares denote the experimental data of Hippler et al.,[14] the circles and crosses of Slagle et al.,[15] and the triangles of Walter et al.[16] The lines denote the present theoretical results for various $\langle \Delta E_{down} \rangle$ values.

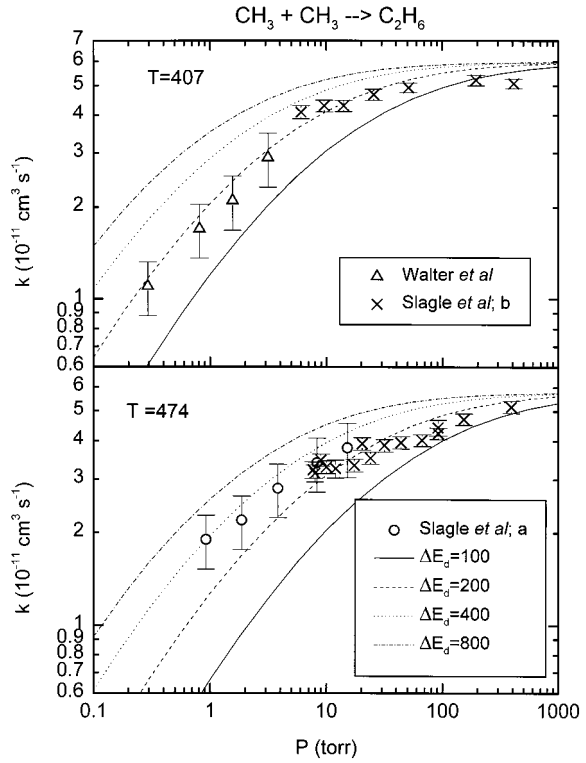

Figure 9. As in Figure 8, but for temperatures of 407 and 474 K.

and vibrational frequencies in place of those for the reference geometries yielded an increase in the transitional mode canonical partition function at 3000 K of only 10%, which is certainly less than the uncertainty arising from the limited sampling. The smallness of this correction suggests that the orientation dependence of the corrections is relatively minor.

IV. Kinetics Results

A. Pressure Dependence. Illustrative plots of the pressure dependence of the bimolecular rate constants are provided in Figures 8−14. In each case, the available experimental data are plotted along with the theoretical predictions for $\langle \Delta E_{down} \rangle$ values of 100, 200, 400, and 800 cm^{-1}. At 200 K (cf. Figure 8) both the absolute rate constants and the predicted negligible dependence on pressure above 10 Torr are in good agreement with the experimental observations.

At 296 K (cf. Figure 8) the experimental pressure range extends to low enough pressures (i.e., 0.1 Torr) to produce a falloff in the rate constant (from its infinite pressure limit) by a factor of 4. The theoretical predictions for energy transfer coefficients $\langle \Delta E_{down} \rangle$ ranging from about 100 to 200 cm^{-1} are in quantitative agreement with the observations. Higher energy transfer coefficients do not produce sufficient falloff in the rate constant with decreasing pressure.

At 407 K (cf. Figure 9) the optimum agreement between theory and experiment occurs for a $\langle \Delta E_{down} \rangle$ value of about 200 cm^{-1}. At 474 K (cf. Figure 9) the optimum $\langle \Delta E_{down} \rangle$ value is again near 200 cm^{-1}. However, at the latter temperature there is some discrepancy between the theoretical and experimental falloff curves. Furthermore, for both these temperatures, the high-pressure limit of the theoretical predictions appears to lie slightly (i.e., about 10−20%) above the experimental limit.

By 577 K (cf. Figure 10) the experimental measurements at the highest pressures are not quite at the high-pressure limit. Regardless, the theoretical predictions now appear to lie measurably above the experimental measurements at the highest pressures, perhaps by about 30%. The optimum agreement between theory and experiment is not very good and now occurs for $\langle \Delta E_{down} \rangle$ values of 200−400 cm^{-1}.

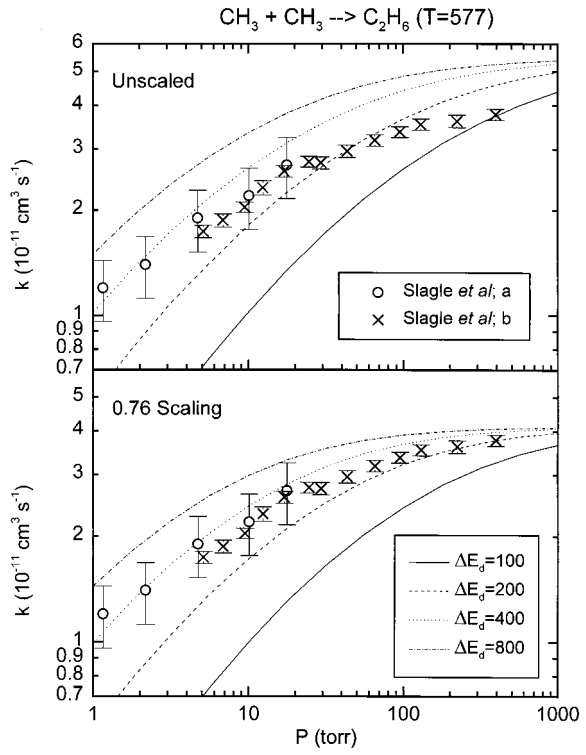

Figure 10. As in Figure 8, but for a temperature of 577 K. The theoretical results in the lower plot employ a transition state number of states which are scaled to yield a high-pressure thermal rate constant which is 0.76 times as large. The upper plot provides the unscaled theoretical results.

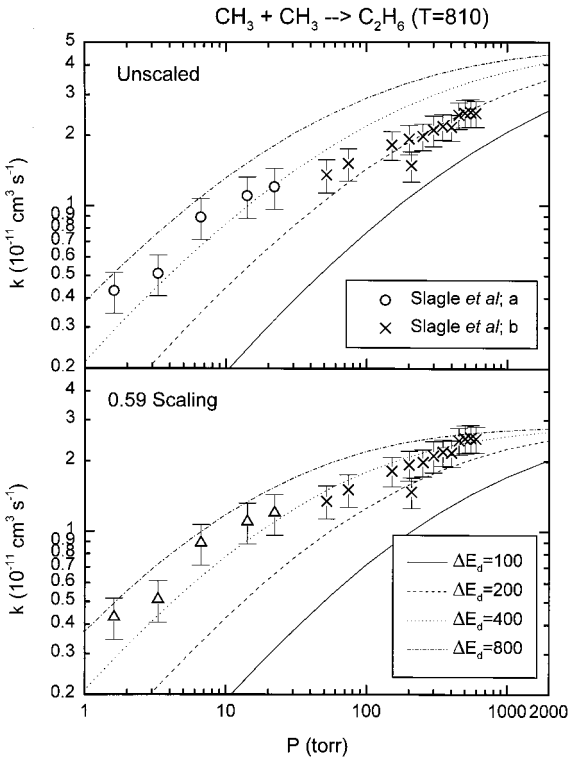

Figure 11. As in Figure 10, but for a temperature of 810 K. At this temperature the scaling reduces the high-pressure thermal rate constant by a factor of 0.59.

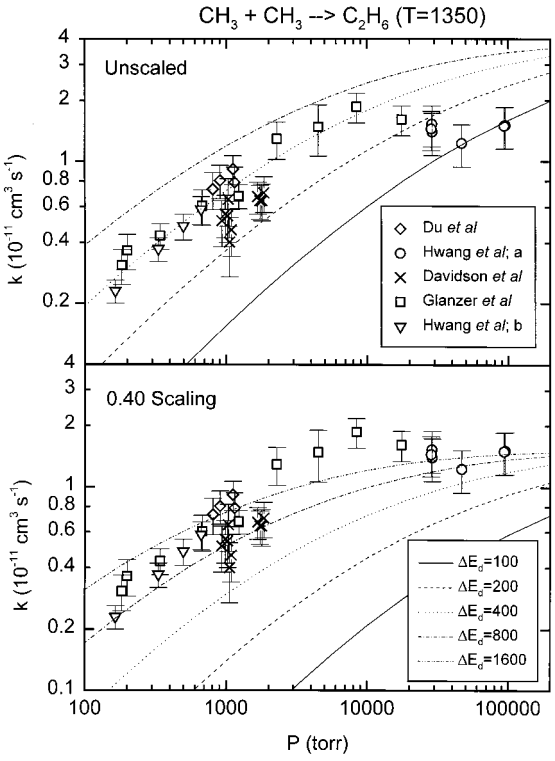

Figure 12. As in Figure 10, but for a temperature of 1350 K, and for different sets of experimental data. The diamonds denote the experimental data of Du et al.,[20] the circles of Hwang et al.,[17] the crosses of Davidson et al.,[19] the squares of Glanzer et al.,[13] and the triangles of Hwang et al.[18] At this temperature the scaling reduces the high-pressure thermal rate constant by a factor of 0.40.

These discrepancies between the theoretical and experimental predictions could be indicative of various errors. Either the theoretical predictions or the experimental measurements for the high-pressure limit may simply be slightly inaccurate. Alternatively, the particular model employed here for the pressure dependence of the kinetics (i.e., the exponential down model for energy transfer within the one-dimensional master equation) may be inadequate. It is instructive to consider to what extent the theoretical predictions for the high-pressure limit would need to be in error in order to obtain a satisfactory reproduction of the experimental observations. Thus, for temperatures of 577 K and higher we have also plotted theoretical predictions for the pressure dependence which employ an energy-dependent scaling of the transition state number of states. This empirical scaling takes the form $[1 - 0.65 \tan h(E/3500)^2]$, where E is the excess energy relative to the dissociation threshold in cm^{-1}. This form, which varies from no correction at low temperature to a maximum correction of 0.35 at high temperature, has no fundamental physical basis. Instead, it was simply designed to produce an average scaling which increases with temperature and to an extent which yields improved agreement with the experimental results for the full range of temperatures considered here. The scale factors printed on the plots indicate the effect of this scaling on the thermal high-pressure limit rate constant for the given temperature. Implementing this scaling for 577 K clearly improves the agreement between theory and experiment.

At 810 K (cf. Figure 11) this empirical scaling results in good agreement between theory and experiment for a $\langle \Delta E_{down} \rangle$ value of about 400 cm^{-1}. In contrast, the optimum falloff curve for the unscaled theoretical result differs signifcantly from the experimental results. At temperatures of 474 and 407 K the thermal scale factors of 0.83 and 0.88, arising from this same energy-dependent scaling, also result in improved agreement between the theoretical and experimental observations. Although not plotted here, this same improvement in the agreement between the theoretical and experimental falloff curves is found for the scaled results for other temperatures in this region (e.g., 700 and 910 K).

A similar situation exists for the higher temperatures of 1200, 1350, 1525, and 1700 K (cf. Figures 12−14). However, for these temperatures the scatter in the experimental data is somewhat greater, and the rate constants for the highest pressures studied appear to be further from the high-pressure limit. As a result, the comparison between the theoretical and experimental results is less definitive. Nevertheless, the scaled results still show a marked improvement in the overall agreement. For these scaled results the optimum $\langle \Delta E_{down} \rangle$ value is near 800 cm^{-1}.

The present pressure-dependent calculations are restricted to temperatures of 1700 K and below, since additional dissociative processes (i.e., to $C_2H_5 + H$, and $C_2H_4 + H_2$) begin to contribute above this range. The potential energy surface and kinetic estimates generated in our study of the $H + C_2H_5$ radical reaction[54] could be employed in an extension of this work to such higher temperatures. However, this extension is sufficiently time consuming that we have chosen to leave it for future work.

B. *T* Dependence of k_∞. A priori VRC-TST predictions for the temperature dependence of the high-pressure limiting rate constant, $k_\infty(T)$, were performed for a somewhat wider temperature range of 200−3000 K. However, the region from 300 to 1700 K is of primary interest and thus our discussion again focuses on this temperature region. The results of these calculations are provided in Table 1 and plotted in Figure 15, together with some related theoretical estimates.

Also plotted in Figure 15 are the corresponding experimental data[14−16] for temperatures of 407 K and lower, where the extrapolation to the high-pressure limit is reasonably secure (cf.

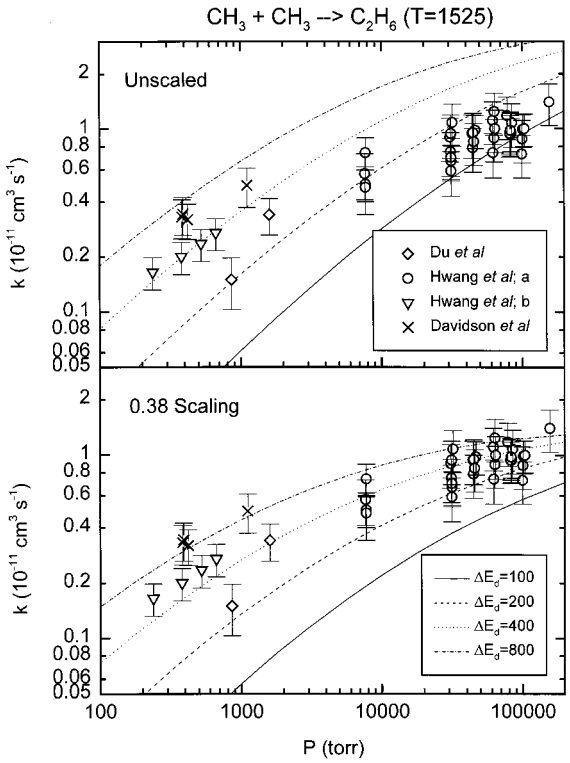

Figure 13. As in Figure 12, but for a temperature of 1525 K. At this temperature the scaling reduces the high-pressure thermal rate constant by a factor of 0.38.

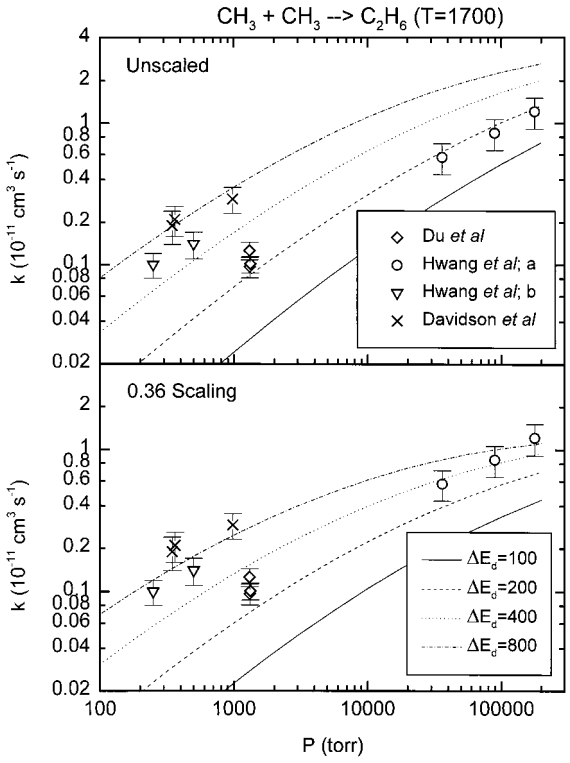

Figure 14. As in Figure 12, but for a temperature of 1700 K. At this temperature the scaling reduces the high-pressure thermal rate constant by a factor of 0.36.

Figures 8−14). For these temperatures, the agreement between the present a priori VRC-TST estimates and the experimental data is remarkable. Unfortunately, as discussed above, the results for the pressure dependence at higher temperatures suggest that this agreement does not persist.

TABLE 1. High-Pressure Association Rate Constants

T (K)	k (10^{-11} cm^3 s^{-1})	T (K)	k (10^{-11} cm^3 s^{-1})
200	6.44	906	4.44
245	6.4	1050	4.22
296	6.28	1200	4.04
370	6.06	1350	3.88
407	5.93	1525	3.74
474	5.7	1700	3.6
513	5.55	1950	3.43
539	5.46	2250	3.24
577	5.31	2600	3.05
700	4.92	3000	2.8
810	4.64		

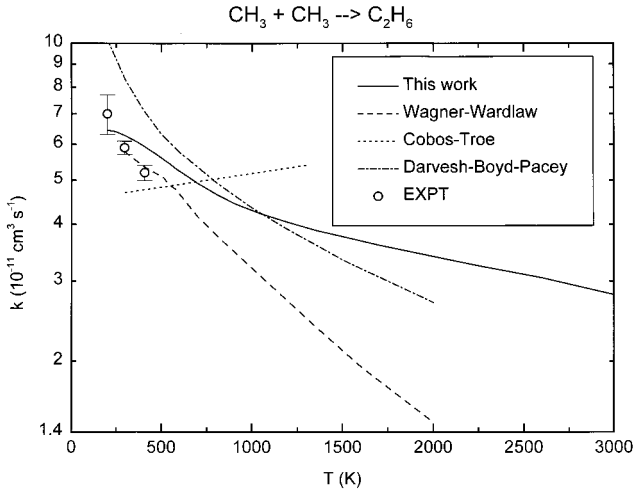

Figure 15. Plot of the temperature dependence of the high-pressure limiting rate constant for methyl radical association. The solid, the dashed, and the dashed−dotted lines represent the TST calculations from this work, from ref 28, and from ref 30. The dotted line denotes the SACM calculations from ref 23. The circles denote the experimental results from refs 14−16.

A variety of other theoretical results are also plotted in Figure 15. The study of Pacey and co-workers[30] is based on a TST method similar to the present one, but employs a potential based on a fit to a limited set of ab initio data. Perhaps not surprisingly, their results are similar to the present ones.

The study of Wagner and Wardlaw[28] is based on an earlier TST-based study of Wardlaw and Marcus.[25] The primary difference between these studies[25,28] and that of Pacey and co-workers[30] is in the use of a more empirical potential energy surface. A key parameter in the study of Wagner and Wardlaw was adjusted to allow their RRKM based calculations to accurately reproduce the pressure-dependent rate constants from ref 15. Thus, the discrepancy between the present results and those of ref 28 is another indication of our apparent overestimate of the high-pressure limit rate constant for high temperatures. Although not shown here, the hindered Gorin model calculations of ref 31 are similar to those of Wagner and Wardlaw.

Cobos and Troe[23] have provided empirical statistical adiabatic channel model (SACM) results which are clearly the most distinctly different from the present ones. In these SACM calculations the α and β parameters that characterize the potential were adjusted to produce a small rise in the high-pressure rate constant with increasing temperature. In contrast, the present a priori TST calculations suggest a decrease by a factor of 1.7 from 300 to 1700 K. Due to the difficulty of measuring the high-pressure limit at temperatures above 500 K, it is currently not possible to resolve the question of the temperature dependence of k_∞ from experimental data alone.

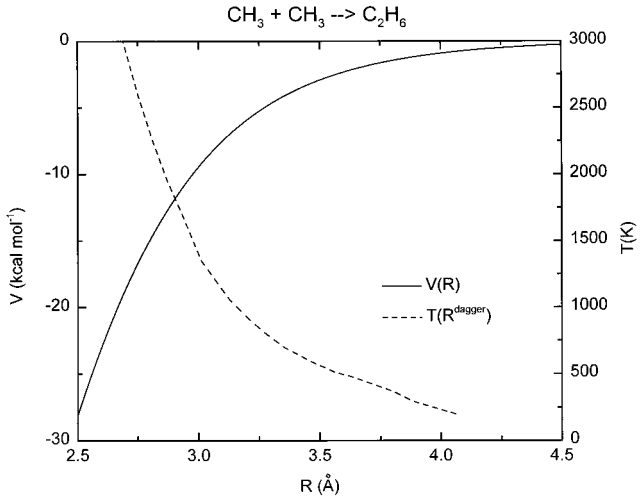

Figure 16. Plot of the temperature dependence of the transition state location (dashed line; right axis) and the interaction potential along the reaction path (solid line; left axis).

The sign and the magnitude of this temperature dependence for radical radical recombinations are of considerable fundamental interest. The separation into the conserved and transitional modes allows one to consider the individual contributions to this temperature dependence. Considering only the transitional modes (i.e., ignoring both the effect of the geometric relaxation of the methyl radicals on the energies and the variations of the methyl radical vibrational frequencies) leads to a predicted drop by a factor of 2.9 over this same temperature range. This drop is due to the increasing hindrance of the relative orientational motions of the two fragments as the interfragment separation decreases.

The conserved mode variations have two competing effects on the temperature dependence. The relaxation energy (arising from the geometric relaxation of the internal coordinates of the methyl radicals) yields a rise in the rate constant by a factor of 2.2 over this temperature range, while the variation in their frequencies leads to a decrease by a factor of 1.3. The umbrella mode is the dominant component in both these variations. The net effect of the conserved mode variations corresponds to an increase by a factor of 1.7 from 300 to 1700 K.

The variation of the CC separation at the transition state with temperature is illustrated in Figure 16. The results plotted therein are for the optimum CC separation with the pivot points 0.4 Å away from the C atoms. The canonical rate constants for the center-of-mass pivot points were generally higher, but only by a few percent. The transition state location is seen to decrease quite dramatically with decreasing separation, decreasing from about 4.0 Å near room temperature to 3.0 Å near 1500 K. The minimum-energy path potential at these separations is remarkably large.

The present calculations have focused on the contribution from solely the ground singlet state. The lowest triplet state is asymptotically degenerate with the ground singlet state. Thus, at large separations, the triplet state may make a nonnegligible contribution to the reactive flux. The size of this contribution is limited in part by the rate of intersystem crossing to the ground singlet state. The maximum contribution would arise for rapid electronic equilibration throughout the transition state region. In this instance, the transition state number of states may be equated with the minimum in the sum of the number of available states for motion on both the singlet and triplet states, including an electronic degeneracy factor of 3 for the triplet state:

$$N^{\dagger}_{EJ} = \min\{N_{EJ}(V_{\text{singlet}}, R) + 3N_{EJ}(V_{\text{triplet}}, R); R\} \quad (6)$$

The evaluation of the triplet potential along the reaction path (cf. Figure 7) allows for a crude estimate of the maximum contribution from the triplet state. This estimate employed a triplet state potential given by the sum of the orientation-dependent singlet state potential and the orientation-independent singlet−triplet splitting along the reaction path. This maximum contribution decreases from 60% of the singlet state contribution at 200 K to 40% at 300 K and 20% at 500 K, and continues to decrease with increasing temperature. The good agreement observed between theory and experiment for the singlet rate near room temperature suggests that the triplet state contribution is likely much smaller due to a slow intersystem crossing rate. Similar observations were made for the H + ethyl and H + vinyl reactions.

The primary results here employ both a Davidson correction for multiple excitations and an orientation-independent reaction path basis set correction. The effect of these corrections provides some indication of the uncertainties due to the accuracy of the ab initio potential. Neglecting the basis set correction yielded rate constants which were 25−40% lower. Further basis set corrections would be expected to yield substantially smaller corrections. The calculations employ an unnormalized Davidson correction which has the effect of increasing the rate by 20−30%. A rough estimate of the probable error in this correction can be made by repeating the calculations using a normalized Davidson correction (unnormalized Davidson corrections typically underestimate the effect of higher order correlations while normalized Davidson corrections often overestimate the importance of these effects). In this case, using the normalized Davidson correction increases the rate by 3−7% relative to using the unnormalized Davidson correction.

V. Concluding Remarks

The direct implementation of 14 600 ab initio data points within a phase space integral based version of VTST yields high-pressure bimolecular rate constants, $k_\infty(T)$, which are in quantitative agreement with experiment near room temperature. The generation of this many data points yields Monte Carlo integration uncertainties on the order of 10% or less for each of the transition state dividing surfaces considered. The underlying quantum chemical estimates are based on calculations at the CAS+1+2/cc-pvdz level but also include corrections for basis set limitations and higher level excitations. The modest variations for neglect of basis set corrections and/or Davidson corrections suggest that any errors in the quantum chemical estimates are likely of only minor importance.

The present a priori theoretical estimates provide strong evidence for a decrease in $k_\infty(T)$ with increasing temperature. The increasing hindrance of the relative orientational modes is the dominant factor in this decrease which amounts to an overall decrease by a factor of 1.7 from 300 to 1700 K. Changes in the umbrella mode geometry and vibrational frequency actually yield a contribution which increases with temperature.

The theoretical and experimental results for the pressure dependence of the bimolecular rate become increasingly discordant as the temperature rises. Such discrepancies may be indicative of failures in either the model for the pressure dependence or of an overestimate of $k_\infty(T)$ at higher temperatures. Sample calculations illustrated that the latter explanation would require an overestimate by about a factor of 2−3 for temperatures of about 1200−1700 K. An empirical reduction of the underlying transition state number of states yielded

pressure-dependent rate constants which were in good agreement with the experimental data.

It is interesting to consider the possible failures in the theoretical calculations which might lead to such an overestimate of $k_\infty(T)$. One possibility is simply that the underlying quantum chemistry is not accurate enough. However, the basis set and Davidson corrections are small enough to suggest that this is unlikely. Alternatively, the transition state evaluations may not be accurate enough. For example, the coupling of the conserved and transitional modes becomes more important as the temperature rises. This coupling has been approximately accounted for via the incorporation of the geometrical relaxation effects and the variation of the conserved mode frequencies along the reaction path. However, such corrections may be inadequate. The consideration of only two different forms for the transition state dividing surface might also lead to some overestimate of the association rate constant. The present model for the pressure dependence of the kinetics may also be inadequate.

Each of the above-mentioned inadequacies, while not necessarily insignificant, do not seem likely to yield the necessary major corrections. An intriguing alternative possibility is that the fraction of trajectories which are directly repulsive increases with temperature ultimately becoming the dominant fraction. These directly repulsive trajectories would be high collision energy trajectories which come in to a close separation and then immediately turn around and dissociate back to reactants. Such trajectories would cross any configuration-based dividing surface and thus result in an overestimate of the effective association rate constant. In the true infinite pressure limit, such trajectories could also be stabilized. However, the immediacy of their return suggests that such stabilization would generally not arise for realistic experimental pressure ranges. The $H + O_2$ reaction provides an interesting example of a case where such trajectories do appear to occupy a major fraction of phase space.[55,56] An empirical model for correcting for the effect of such repulsive trajectories has been provided by Truhlar.[57]

Acknowledgment. This work was supported by the U.S. Department of Energy, Office of Basic Energy Sciences, Division of Chemical Sciences, under Contract W-31-109-ENG-38 (L.B.H. and S.J.K.) and through NSF grant CHE-9423725 (S.J.K.). Helpful discussions with Jan Hessler, Al Wagner, and Dave Wardlaw are gratefully acknowledged.

References and Notes

(1) Helgaker, T.; Uggerud, E.; Jensen, H. J. A. *Chem. Phys. Lett.* **1990**, *173*, 145.

(2) Hartke, B.; Carter, E. A. *Chem. Phys. Lett.* **1992**, *189*, 358.

(3) Chen, W.; Hase, W. L.; Schlegel, H. B. *Chem. Phys. Lett.* **1994**, *228*, 436.

(4) Collins, M. A.; *Adv. Chem. Phys.* **1996**, *93*, 389. Bettens, R. P. A.; Collins, M. A. *J. Chem. Phys.* **1998**, *109*, 9728.

(5) Schatz, G. C.; Papaioannou, A.; Pederson, L. A.; Harding, L. B.; Hollebeek, T.; Ho, T. S.; Rabitz, H. *J. Chem. Phys.* **1997**, *107*, 2340. Ho, T. S.; Hollebeek, T.; Rabitz, H.; Harding, L. B.; Schatz, G. C.; *J. Chem. Phys.* **1996**, *105*, 10472.

(6) Truhlar, D. G. In *The Reaction Path in Chemistry: Current Approaches and Perspectives*; Heidrich, D., Ed.; Kluwer: Dordrecht, The Netherlands, 1995; pp 229−255.

(7) Duncan, W. T.; Bell, R. L.; Truong, T. N. *J. Comput. Chem.* **1998**, *19*, 1039. Truong, T. N.; Duncan, W. T.; Bell, R. L. *ACS Symp. Ser.* **1996** *629*, 85.

(8) Wardlaw, D. M.; Marcus, R. A. *Adv. Chem. Phys.* **1988**, *70*, Part 2, 231.

(9) Klippenstein, S. J. In *Advances in Physical Chemistry: The Chemical Dynamics and Kinetics of Small Radicals*; Liu, K., Wagner, A. F., Eds.; World Scientific: Singapore, 1995; Part 1.

(10) Klippenstein, S. J.; Allen, W. D. *Ber. Bunsen. Phys. Chem.* **1997**, *101*, 423. Klippenstein, S. J.; East, A. L. L.; Allen, W. D. *J. Chem. Phys.* **1996** *105*, 118.

(11) Mallard, W. G. NIST Chemical Kinetics Database, 1992, and references therein.

(12) Glänzer, K.; Quack, M.; Troe, J. *Chem. Phys. Lett.* **1976**, *39*, 304.

(13) Glänzer, K.; Quack, M.; Troe, J. In *Sixteenth Symposium (International) Combustion*; The Combustion Institute: Seattle, WA, 1977; p 949.

(14) Hippler, H.; Luther, K.; Ravishankara, A. R.; Troe, J. *Z. Phys. Chem. NF* **1984**, *142*, 1.

(15) Slagle, I. R.; Gutman, D.; Davies, J. W.; Pilling, M. J. *J. Phys. Chem.* **1988**, *92*, 2455.

(16) Walter, D.; Grotheer, H.-H.; Davies, J. W.; Pilling, M. J.; Wagner, A. F. In *Twenty-Third Symp. (Int.) Combust.;* The Combustion Institute: Seattle, WA; 1990; p 107.

(17) Hwang, S. M.; Wagner, H. G.; Wolff, T. In *Twenty-Third Symp. (Int.) Combust.;* The Combustion Institute: Seattle, WA, 1990; p 99.

(18) Hwang, S. M.; Rabinowitz, M. J.; Gardiner, Jr., W. C. *Chem. Phys. Lett.* **1993**, *205*, 157.

(19) Davidson, D. F.; DiRosa, M. D.; Chang, E. J.; Hanson, R. K.; Bowman, C. T. *Int. J. Chem. Kinet.* **1995**, *27*, 1179.

(20) Du, H.; Hessler, J. P.; Ogren, P. J. *J. Phys. Chem.* **1996**, *100*, 974.

(21) Gorin, E. *J. Chem. Phys.* **1939**, *7*, 256.

(22) Quack, M.; Troe, J. *Ber. Bunsen-Ges. Phys. Chem.* **1977**, *81*, 329.

(23) Cobos, C. J.; Troe, J. *J. Chem. Phys.* **1985**, *83*, 1010.

(24) Wardlaw, D. M.; Marcus, R. A. *J. Chem. Phys.* **1985**, *83*, 3462.

(25) Wardlaw, D. M.; Marcus, R. A. *J. Phys. Chem.* **1986**, *90*, 5383.

(26) Evleth, E. M.; Kassab, E. *Chem. Phys. Lett.* **1986**, *131*, 475.

(27) Klippenstein, S. J.; Marcus, R. A. *J. Chem. Phys.* **1987**, *87*, 3410.

(28) Wagner, A. F.; Wardlaw, D. M. *J. Phys. Chem.* **1988**, *92*, 2462.

(29) Smith, S. C.; Gilbert, R. G. *Int. J. Chem. Kinet.* **1988**, *20*, 307, 979.

(30) Darvesh, K. V.; Boyd, R. J.; Pacey, P. D. *J. Phys. Chem.* **1989**, *93*, 4772.

(31) Stewart, P. H.; Larson, C. W.; Golden, D. M. *Combust. Flame* **1989**, *75*, 25.

(32) Aubanel, E. E.; Robertson, S. H.; Wardlaw, D. M. *J. Chem. Soc., Faraday Trans.* **1991**, *87*, 2291.

(33) Forst, W. *J. Phys. Chem.* **1991**, *95*, 3612.

(34) Robertson, S. H.; Wardlaw, D. M.; Hirst, D. M. *J. Chem. Phys.* **1993**, *99*, 7748.

(35) Pitt, I. G.; Gilbert, R. G.; Ryan, K. R. *J. Phys. Chem.* **1995**, *99*, 239.

(36) Robertson, S. H.; Pilling, M. J.; Baulch, D. L.; Green, N. J. B. *J. Phys. Chem.* **1995**, *99*, 13452.

(37) Hessler, J. P.; Ogren, P. J. *J. Phys. Chem.* **1996**, *100*, 984.

(38) Hessler, J. P. *J. Phys. Chem.* **1996**, *100*, 2141.

(39) Jeffrey, S. J.; Gates, K. E.; Smith, S. C. *J. Phys. Chem.* **1996**, *100*, 7090.

(40) Pesa, M.; Pilling, M. J.; Robertson, S. H.; Wardlaw, D. M. *J. Phys. Chem. A* **1998**, *102*, 8526.

(41) Pacey, P. D. *J. Phys. Chem. A* **1998**, *102*, 8541.

(42) Naroznik, M. *J. Chem. Soc., Faraday Trans.* **1998**, *94*, 2531.

(43) The experimental data for temperatures greater than about 1700 K (cf. ref 19 and references therein) includes a significant contribution from the $H + C_2H_5$ channel and thus will not be considered here.

(44) Klippenstein, S. J. *Chem. Phys. Lett.* **1990**, *170*, 71; *J. Chem. Phys.* **1991**, *94*, 6469; **1992**, *96*, 367.

(45) Klippenstein, S. J. *J. Phys. Chem.* **1994**, *98*, 11459.

(46) Dunning, T. H., Jr. *J. Chem. Phys.* **1989**, *90*, 1007.

(47) Kendall, R. A.; Dunning, T. H., Jr.; Harrison, R. J. *J. Chem. Phys.* **1992**, *96*, 6796.

(48) Woon, D. E.; Dunning, T. H., Jr. *J. Chem. Phys.* **1993**, *98*, 1358.

(49) Langhoff, S. R.; Davidson, E. R. *Int. J. Quantum Chem.* **1974**, *8*, 61. Silver, D. W.; Davidson, E. R. *Chem. Phys. Lett.* **1978**, *52*, 403.

(50) Shepard, R.; Shavitt, I.; Pitzer, R. M.; Comeau, D. C.; Pepper, M.; Lischka, H.; Szalay, P. G.; Ahlrichs, R.; Brown, F. B.; Zhao, J.-G. *Int. J. Quantum Chem.* **1988**, *S22*, 149.

(51) Gilbert, R. G.; Smith, S. C. *Theory of Unimolecular Recombination Reactions*, Blackwell Scientific: Oxford, UK, 1990; Holbrook, R. A.; Pilling, M. J.; Robertson. S. H. *Unimolecular Reactions*, 2nd ed.; Wiley: Chichester, UK, 1996.

(52) Robertson, S. H.; Pilling, M. J.; Baulch, D. L.; Green, N. J. B. *J. Phys. Chem.* **1995**, *99*, 13452.

(53) Yu, J.; Klippenstein, S. J. *J. Phys. Chem.* **1991**, *95*, 9882.

(54) Harding, L. B.; Klippenstein, S. J. *27th Symp. (Int.) Combust.* **1998**, 151.

(55) Yang, C.-Y.; Klippenstein, S. J. *J. Chem. Phys.* **1995**, *103*, 7287.

(56) Dobbyn, A. J.; Stumpf, M.; Keller, H.-M.; Schinke, R. *J. Chem. Phys.* **1996**, *104*, 8357.

(57) Truhlar, D. G. *J. Am. Chem. Soc.* **1975**, *97*, 6310.